



## PAPER

## Characterization of normal and deformed red blood cells using simulated differential photoacoustic cross-section spectral data

## OPEN ACCESS

## RECEIVED

16 November 2020

## REVISED

2 March 2021

## ACCEPTED FOR PUBLICATION

3 March 2021

## PUBLISHED

12 March 2021

Original content from this work may be used under the terms of the [Creative Commons Attribution 4.0 licence](https://creativecommons.org/licenses/by/4.0/).

Any further distribution of this work must maintain attribution to the author(s) and the title of the work, journal citation and DOI.



Anuj Kaushik and Ratan K Saha\*

Department of Applied Sciences, Indian Institute of Information Technology Allahabad, Jhalwa, Prayagraj, 211015, India

\* Author to whom any correspondence should be addressed.

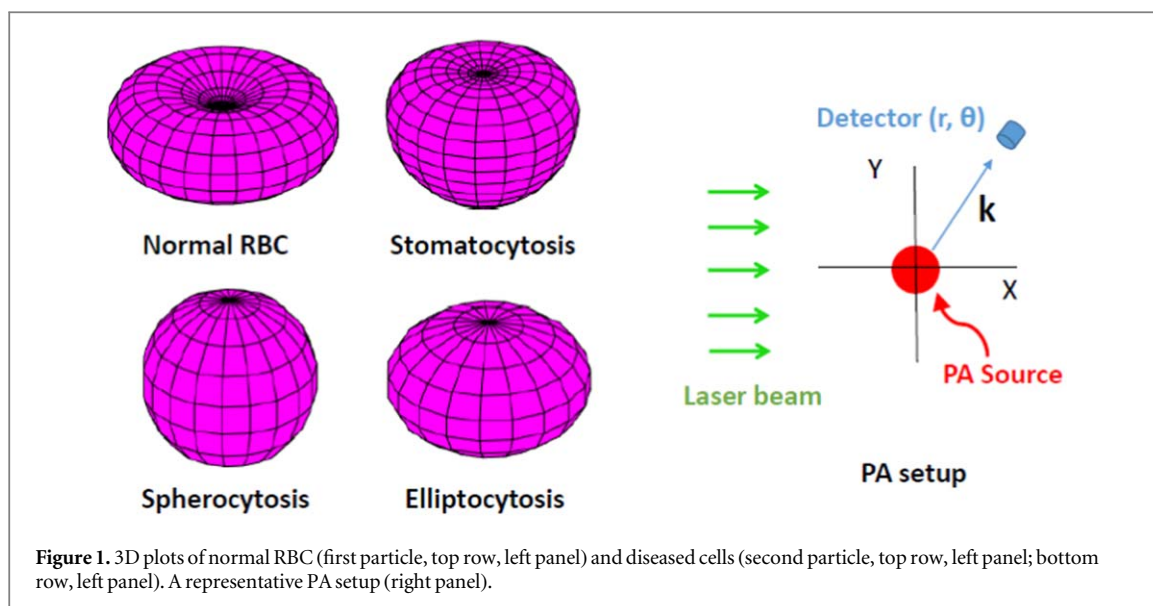
E-mail: [rss2017503@iiita.ac.in](mailto:rss2017503@iiita.ac.in) and [ratank.saha@iiita.ac.in](mailto:ratank.saha@iiita.ac.in)**Keywords:** medical and biomedical optics, cytometry, cell characterization, differential photoacoustic cross-section, Green's function, spectrum analysis**Abstract**

Frequency dependent differential photoacoustic cross-section (DPACS) over a large frequency band (100–1000 MHz) has been computed and subsequently, morphological parameters of photoacoustic (PA) source have been quantified. Green's function method has been employed for computing the DPACS for a series of ellipsoidal droplets (with varying aspect ratio), Chebyshev particles (with different waviness ( $n$ ) and deformation ( $\epsilon$ ) parameters), healthy red blood cell (RBC) and cells suffering from hereditary disorders (spherocytosis, elliptocytosis and stomatocytosis). The tri-axial ellipsoid form factor (TAEFF), finite cylinder form factor (CFF) and toroid form factor (TFF) models have been used to fit the DPACS spectrum to obtain size and shape information of the PA source. The TAEFF model estimates the shape parameters of the ellipsoidal droplets accurately (error  $< 5\%$ ). It is found that volume estimation is better (error  $< 10\%$ ) for lower order ( $n = 2$ ,  $\epsilon = \pm 0.25$ ) and very higher order ( $n = 35, 45$ ,  $\epsilon = \pm 0.05$ ) Chebyshev particles compared to those of  $n = 4, 6$  and  $\epsilon = \pm 0.25$ . The TAEFF model predicts shape parameters of stomatocyte with volume error  $\approx 15\%$  but it is  $\leq 6\%$  for other cells. The opposite trend is observed for the CFF model. The TFF model is able to estimate the shape parameters efficiently for normal erythrocyte and stomatocyte but gives relatively large errors ( $> 15\%$ ) for other deformed RBCs. The inverse problem framework may motivate to develop a PA-based technology to assess single cell morphology.

**1. Introduction**

Photoacoustic (PA) effect depends on the principle of thermal expansion and contraction. When a pulsed laser beam comes in contact with the light absorbing particles suspended in a fluidic system a definite amount of energy is devolved to the cell/tissue in the form of heat. The heating effect increases the temperature of the particles and makes them expand. On the other hand, removal of the laser radiation lowers down the temperature of the particles and they contract. When the phenomenon of expansion and contraction is done in a fast-enough manner, cell/tissue will produce pressure waves that can eventually be received by a detector [1–3]. The characteristics of the PA signals depend upon various key parameters of the cell/tissue. In other words, physical/morphological properties of the source can be quantified by analyzing the PA signals. For example, a PA tomography image, formed utilizing the measured PA signals, can accurately display spatial distribution of various tissue parameters (e.g., hemoglobin concentration, oxygen saturation level etc.) [4, 5]. PA tomography has found important applications ranging from brain imaging, vasculature imaging, breast imaging, sentinel lymph node imaging and molecular imaging [4, 5].

Numerous researchers have effectively recorded the PA signals from single cells. The PA signals were successfully captured by Galaza *et al* from sickled cells, circulatory tumor cells and malaria infected cells in blood stream *in vivo* [1–3]. They employed diagnostic ultrasound detectors ( $\approx 3.5$  to 20 MHz) for this purpose. Strohm *et al*, deployed ultra-high frequency transducers (few hundred MHz to GHz) to measure the PA signals from normal



and defective red blood cells (RBCs) [6, 7]. The nucleus to cytoplasmic ratio of cancer cells has also been calculated by analyzing the measured PA signals [8]. The quantitative estimation of this parameter can aid in assessing cell malignancy. They demonstrated that PA spectral features above 100 MHz depend upon the shape and size parameters of the light absorbing cells [6, 7]. The final goal of these research works is to develop PA flow cytometry technology for *in vivo* characterization of deformed RBCs in blood vessel to detect and fight lethal disorders.

Normal erythrocytes are incredibly deformable and stable which empower them to go through vessels and perform standard physiological activities [9]. An erythrocyte does not have any core and shows up as a biconcave plate. This specific shape provides large surface-to-volume proportion (i.e.,  $S/V$ ) which helps RBCs to function effectively. Hereditary issues, irresistible illness, infections and change in blood chemistry can induce change in shape of erythrocyte and also hinder its capacity to twist and deform [10]. The irreversible deformation in the morphology of RBCs blocks blood flow causing tissue necrosis [6]. Aside from above ailments, there are a few genetic issues for which erythrocytes cannot maintain the discocyte shape [11]. The examples include hereditary spherocytosis, elliptocytosis and stomatocytosis [9, 11, 12]. Representative plots of these cells are displayed in figure 1 (left panel). It may be mentioned here that for the Caucasian race, one out of 2000 population is experiencing genetic spherocytosis and elliptocytosis illnesses. In these cases, the cohesion between the lipid bilayer and cytoskeleton is reduced by the film proteins or clearness of cytoskeleton. As a result of that surface to volume ratio ( $S/V$ ) decreases and it also induces permanent morphological changes [9]. Diseased RBCs are perceived as ailing cells by the spleen and hence, are pulled out from the circulation directing to the hemolytic anemia. Note that spleen is the secondary immune organ of the human body. Light-scattering or electrical impedance techniques have been extensively used to determine the RBC concentration and mean corpuscular volume [13–15]. Blood smear microscopic examination, ektacytometry, and cytology techniques can also detect hemolytic anemia, by differentiating the morphology of the erythrocytes. These methods are difficult and time taking. Moreover, moderate spherocytosis or elliptocytosis are hard to detect by the cytology technique and arduous too. The PA technique may be evolved as a suitable method without having these drawbacks.

We have examined in detail how differential PA cross-section (DPACS) vary with the shape and size of a source [16–19]. The DPACS is defined as the acoustic power received by a detector situated in the far field with respect to the source per unit solid angle divided by the intensity of the incident light beam. The Green's function method has been applied to compute the pressure field generated by a cell/particle of use and subsequently, DPACS has been estimated. This quantity can be contrasted with the differential scattering cross-section which has been examined extensively in numerous fields to characterize the scattering center. We investigated how the PA spectrum vary for a number of particles (i.e., spheroidal droplets with different aspect ratio (AR), Chebyshev particles with different deformation ( $\epsilon$ ) and waviness ( $n$ ) parameters, healthy and diseased RBCs [16]. The angular distribution of DPACS at 390 MHz was studied for cells. Such curves were then fitted using the tri-axial ellipsoid form factor (TAEFF) and cylinder form factor (CFF) models to accomplish morphological characterization of these particles [17, 18]. Recently, a robust theoretical framework accounting various realistic factors is presented by us [19]. It considers that the PA signals are captured by a finite size ultrasonic transducer and the medium from source to the detector is acoustically dispersive and lossy. Encouraging results have been obtained. The PA field emitted by a source having nonvanishing acoustic impedance mismatch (compared to the surrounding medium) has also been computed via the Born series techniques [20, 21]. It was observed that

the traditional Born series method works well when the speed of sound contrast resides within  $-11\%$  to  $22\%$ . However, the convergent Born series technique remains valid even beyond these limits.

The goal of this article is two folds. The alteration of DPACS with frequency (100–1000 MHz) when captured by a point receiver is investigated in the forward framework. Such curves have been generated for three locations  $\theta = 0, \pi/4, \pi/2$  and  $\phi = \pi/4$ . In the inverse problem, fitting of the DPACS plots (for  $\theta = \pi/4$  and  $\phi = \pi/4$ ), produced by the same test objects as stated previously, have been done with form factor models to evaluate the morphological parameters. Apart from two (TAEFF and CFF) simple models, we utilized toroid form factor (TFF) model too for fitting. The derivation of these models is carried out in details in this paper. The performance of these models have been rigorously evaluated for different cells/droplets investigated in this work. Reliable estimation of the shape parameters for ellipsoidal particles is possible by the TAEFF model. The TFF model precisely determines the characteristic size of normal RBC. The CFF model seems to be inferior among them. The models may be utilized to analyze measured spectral data for the evaluation of cell morphology.

The structure of the paper is as follows. Section 2 details the modeling approaches (forward and inverse frameworks). The numerical schemes utilized in this study are elaborated in section 3. The computational results are illustrated in section 4. Section 5 highlights important points regarding the form factor models and how to apply them in future for solving practical problems. The conclusion of this research work is also presented here.

## 2. Modeling approaches

### 2.1. Modeling of the forward problem

The time independent wave equation for PA pressure ( $p$ ) in an acoustically nondispersive and nonabsorbing medium is given by [22],

$$\nabla^2 p + k^2 p = \begin{cases} \frac{i\omega\mu\beta I_0}{C_p}, & \text{inside the source} \\ 0, & \text{outside the source.} \end{cases} \quad (1)$$

Here,  $\beta$  is the specific heat capacity at constant pressure;  $\mu$  is optical absorption coefficient; and  $C_p$  is the isobaric thermal expansion coefficient of the PA source. Further,  $\omega$  and  $I_0$  denote the modulation frequency and intensity of the incident laser beam, respectively; the notation  $k$  represents the wave number. Note that the acoustic characteristics (density and speed of sound) inside and outside the PA source are assumed to be the same. Further, the opto-thermo-mechanical parameters do not exhibit spatial variation within the source region. In deriving equation (1), the conditions of thermal and stress confinements have been imposed. The solution to equation (1) can be derived as [16, 17],

$$p_{\text{ext}}(\mathbf{r}, k) = \int_{V_{\text{vol}}} \frac{i\mu\beta I_0 \omega}{C_p} G(\mathbf{r}|\mathbf{r}_0) d^3 \mathbf{r}_0, \quad (2)$$

where  $V_{\text{vol}}$  refers to the volume of the absorber;  $G(\mathbf{r}|\mathbf{r}_0) = -\frac{e^{ik|\mathbf{r}-\mathbf{r}_0|}}{4\pi|\mathbf{r}-\mathbf{r}_0|}$  alludes the free space Green's function;  $\mathbf{r}_0(r_0, \theta_0, \phi_0)$  is the source point and  $\mathbf{r}(r, \theta, \phi)$  is the field point [23]. A schematic diagram of the PA geometry in 2D is illustrated in the right panel of figure 1. The field point lies outside the absorber (i.e.,  $r > r_0$ ) and that is denoted by the subscript ext. Equation (2) in the far field ( $r \gg r_0$ ) becomes,

$$\begin{aligned} p_{\text{ext}}(\mathbf{r}, k) &\approx -\frac{e^{ikr}}{4\pi r} \frac{i\mu\beta I_0 \omega}{C_p} \int_{V_{\text{vol}}} e^{-ik\mathbf{r}_0} d^3 \mathbf{r}_0 \\ &= -\frac{e^{ikr}}{4\pi r} \frac{i\mu\beta I_0 \omega}{C_p} \Upsilon \\ &= \frac{e^{ikr}}{r} M(\mathbf{k}), \end{aligned} \quad (3)$$

where,

$$\Upsilon = \int_{V_{\text{vol}}} e^{-ik\mathbf{r}_0} d^3 \mathbf{r}_0, \quad (4)$$

and  $M(\mathbf{k}) = -i\mu\beta I_0 \omega \Upsilon / (4\pi C_p)$ , represents the strength of the wave (moving radially outward from the source) emitted by the light absorbing object. Accordingly, the DPACS is calculated as [16, 17],

$$\sigma(k, \theta) = \frac{|M(\mathbf{k})|^2}{2\rho v I_0}. \quad (5)$$

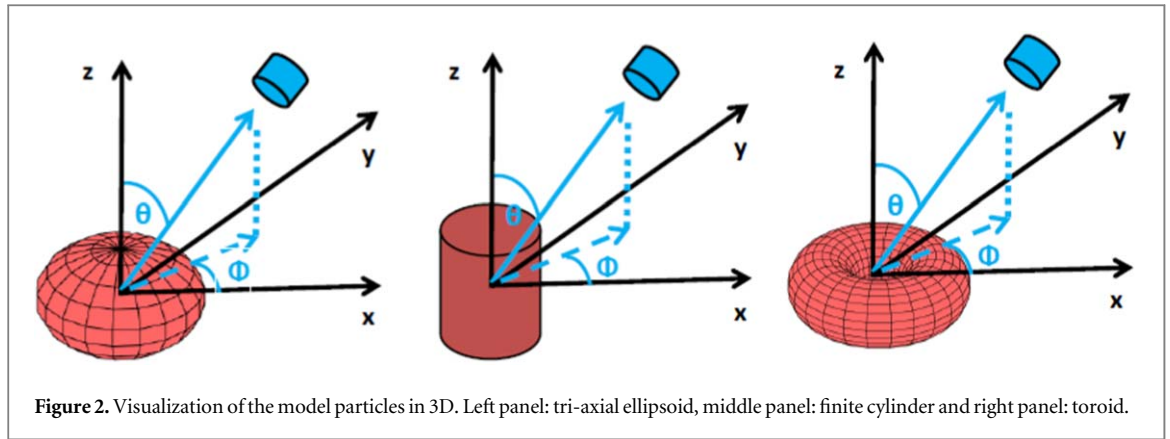


Figure 2. Visualization of the model particles in 3D. Left panel: tri-axial ellipsoid, middle panel: finite cylinder and right panel: toroid.

Here,  $v$  and  $\rho$  denote the speed of sound and density of the ambient fluid medium. The term DPACS has been coined by us. The DPACS is similar to the differential scattering cross-section, which is used frequently and measured in many streams to examine the properties of scatterer. In this study, we have numerically calculated frequency dependent DPACS, equation (5), for various irregular shapes imitating the biological cells.

In this study, PA signals for a delta function heating pulse have also been computed for some shapes by employing the following expression [22],

$$p_{\text{ext}}(\mathbf{r}, t) \approx \frac{i\mu\beta F}{2\pi C_p} \int_{-\infty}^{\infty} \omega e^{-i\omega t} \left[ -\frac{e^{i\mathbf{k}\mathbf{r}}}{4\pi r} \int_{V_{\text{vol}}} e^{-i\mathbf{k}\cdot\mathbf{r}_0} d^3\mathbf{r}_0 \right] d\omega, \quad (6)$$

where  $F$  is the fluence of the incident laser beam. It may be noted that equation (6) represents an analytic signal.

## 2.2. Modeling of the inverse problem

The integration in equation (4) for regular objects (i.e., sphere, infinite cylinder etc.) can be carried out analytically. Hence, simple and elegant closed form formulas for  $\sigma(\mathbf{k})$  can be obtained. For instance, for an ellipsoidal droplet, one derives [24, 25],

$$\begin{aligned} \Upsilon &= \int_{V_{\text{vol}}} e^{-i(k_x x_0 + k_y y_0 + k_z z_0)} dx_0 dy_0 dz_0 \\ &= \frac{\varrho_2 \varrho_3}{\varrho_1^2} \int_{V_{\text{vol}}} e^{-i(k'_x x'_0 + k'_y y'_0 + k'_z z'_0)} dx'_0 dy'_0 dz'_0 \\ &= \frac{4\pi \varrho_1 \varrho_2 \varrho_3}{3} \frac{3j_1(k' \varrho_1)}{k' \varrho_1}. \end{aligned} \quad (7)$$

The following substitutions have been made-  $k'_x = k_x$ ,  $k'_y = k_y \varrho_2 / \varrho_1$ ,  $k'_z = k_z \varrho_3 / \varrho_1$ ,  $x'_0 = x_0$ ,  $y'_0 = \varrho_1 y_0 / \varrho_2$ ,  $z'_0 = \varrho_1 z_0 / \varrho_3$  where  $\varrho_1$ ,  $\varrho_2$  and  $\varrho_3$  indicate the semi-axes of the ellipsoidal droplet, respectively;  $j_1$  is the spherical Bessel function of order unity and  $k' = \frac{k}{\varrho_1} \sqrt{\varrho_1^2 \sin^2 \theta \cos^2 \phi + \varrho_2^2 \sin^2 \theta \sin^2 \phi + \varrho_3^2 \cos^2 \theta}$ . Therefore, equation (5) becomes,

$$\sigma(k, \theta) = \frac{\mu^2 \beta^2 I_0 \omega^2}{2\rho v C_p^2} \frac{V_{\text{vol}}^2}{16\pi^2} FF^2, \quad (8)$$

and

$$FF = 3j_1(k' \varrho_1) / (k' \varrho_1),$$

is called the TAEFF and  $FF \rightarrow 1$  for small particle. Figure 2 (left panel) demonstrates the geometrical setup of an ellipsoidal droplet. It might be stated here that morphological information of the light absorbing region are embedded in  $FF$ . To quantify the size of the scatterer, the  $FF$  models are often used in many fields [24].

In the similar fashion, one for a finite cylinder (see figure 2, middle panel) arrives at [25],

$$\begin{aligned} \Upsilon &= \int_0^\Gamma \int_0^{2\pi} \int_{-\frac{L}{2}}^{\frac{L}{2}} e^{-i(kz_0 \cos \theta + kr_0 \sin \theta \cos \psi_0)} r_0 dr_0 d\psi_0 dz_0 \\ &= \pi \Gamma^2 L \frac{2J_1(k\Gamma \sin \theta)}{k\Gamma \sin \theta} \frac{\sin(k\frac{L}{2} \cos \theta)}{k\frac{L}{2} \cos \theta}, \end{aligned} \quad (9)$$

where  $L$ ,  $\Gamma$  and  $J_1$  symbolize length, radius of the cylinder and the Bessel function of first kind of order one, respectively. Thus, the corresponding formula can be written as,

$$FF = \frac{2J_1(k\Gamma \sin(\theta)) \sin(k\frac{L}{2} \cos(\theta))}{k\Gamma \sin(\theta) k\frac{L}{2} \cos(\theta)}. \quad (10)$$

For a toroidal source, equation (4) may be written as [26, 27],

$$\begin{aligned} \Upsilon &= \int_{-R_c}^{+R_c} \int_0^{2\pi} \int_{R_-}^{R_+} e^{-i[kz_0 \cos \theta + kr_0 \sin \theta \cos \psi_0]} r_0 dr_0 d\psi_0 dz_0 \\ &= 2\pi \int_{-R_c}^{+R_c} [R_+ J_1(kR_+ \sin \theta) - R_- J_1(kR_- \sin \theta)] \\ &\quad \times \frac{\cos(kz_0 \cos \theta)}{k \sin \theta} dz_0, \end{aligned} \quad (11)$$

with  $R_+ = R_t + \sqrt{R_c^2 - z_0^2}$  and  $R_- = R_t - \sqrt{R_c^2 - z_0^2}$ ;  $R_c$  and  $R_t$  are the cross-sectional radius and radius of the toroid, respectively. In this derivation, it is assumed that the plane of the toroid and the  $z$ -axis are perpendicular to each other (see right panel of figure 2). Accordingly, the TFF can be presented as [26, 27],

$$\begin{aligned} FF &= \frac{1}{\pi R_c^2 R_t} \int_{-R_c}^{+R_c} [R_+ J_1(kR_+ \sin \theta) - R_- J_1(kR_- \sin \theta)] \\ &\quad \times \frac{\cos(kz_0 \cos \theta)}{k \sin \theta} dz_0. \end{aligned} \quad (12)$$

These three FF models are utilized herein to fit simulated DPACS spectra for various objects similar to biological cells and to accomplish their morphological characterization. The TAEFF and CFF models are quite simple and thus appealing. The visualization of source morphology is indeed trivial in terms of the best fit parameters ( $\rho_1, \rho_2$  and  $\rho_3$  in case of the TAEFF model;  $\Gamma$  and  $L$  belong to the CFF model), obtained by solving the inverse problem and also interpretation of the extracted parameters becomes easy. The TFF model better resembles normal RBC and that is why it has been utilized in this study.

### 3. Computational method

#### 3.1. Formulas for generating the shapes of various PA sources

The revolution around the major and minor axes of an ellipsoid generates the prolate and oblate spheroids, respectively. The radial and angular coordinates of a point situated on the surface of a spheroid are related to,

$$r'(\theta') = \frac{ab}{[b^2 \sin^2 \theta' + a^2 \cos^2 \theta']^{1/2}}, \quad (13)$$

with  $b$  and  $a$  are the lengths of the semi- minor axis and major axis, respectively.

The shapes that fall under the category of Chebyshev particle can be generated as [28],

$$r'(\theta') = R_c [1 + \epsilon \cos n\theta'], \quad (14)$$

where  $\epsilon$  and  $n$  refer to the deformation and waviness parameters, respectively;  $R_c$  denotes the radius of the unperturbed sphere. Various realistic particles can be approximated as the Chebyshev particles. These objects exhibit symmetry about the  $z$ -axis and nonspherical in shape.

Here, the Cassini oval model was used to construct the shape of normal RBC (see left image of top row of figure 1) and it can be presented as [29],

$$(x^2 + y^2 + z^2 + \eta^2)^2 - 4\eta^2(x^2 + y^2) = \zeta^4. \quad (15)$$

The biconcave shape can be produced with equation (15) when  $\eta$  is slightly less than  $\zeta$ . Further, the  $\eta$  and  $\zeta$  values are related to the four morphological parameters, namely, diameter ( $D$ ), dimple thickness ( $t$ ), maximum thickness ( $h$ ) and the diameter of the circular contour drawn on the maximum thickness ( $d$ ) as,  $D^2 = 4(\zeta^2 + \eta^2)$ ,  $t^2 = 4(\zeta^2 - \eta^2)$  and  $h = \zeta^2/\eta$  [29, 30].

#### 3.2. Choice of thermo-opto-mechanical parameters

The numerical values of the thermo-opto-mechanical parameters for the PA objects were chosen as-  $I_0 = 1.51 \times 10^{12} \text{ Jm}^{-2}\text{s}^{-1}$ ,  $\mu = 809.02 \text{ m}^{-1}$ ,  $\beta = 1.5 \times 10^{-4} \text{ K}^{-1}$ ,  $C_p = 3.23 \times 10^3 \text{ Jkg}^{-1}\text{K}^{-1}$ . The values of speed of sound ( $v = 1498 \text{ m/s}$ ) and density ( $\rho = 1005 \text{ kg m}^{-3}$ ) of the source and ambient media were taken from the literature [17]. The numerical values of these parameters are shown in table 1.

#### 3.3. Choice of the shapes of the PA sources

In this article, we took ellipsoidal droplets with aspect ratio,  $AR = 1:2, 1:4, 1:8, 2:1, 4:1$  and  $8:1$  and Chebyshev particles with deformation parameters  $\epsilon = \pm 0.25$  and waviness parameters,  $n = 2, 3, 8$ . Chebyshev shapes with

**Table 1.** Numerical values of various physical parameters considered in this study.

$\rho$	$1005 \text{ kg m}^{-3}$
$v$	$1498 \text{ m/s}$
$\mu$	$809.02 \text{ m}^{-1}$
$\beta$	$1.5 \times 10^{-4} \text{ K}^{-1}$
$C_p$	$3.23 \times 10^3 \text{ Jkg}^{-1}\text{K}^{-1}$
$I_0$	$1.51 \times 10^{12} \text{ Jm}^{-2}\text{s}^{-1}$

**Table 2.** Quantitative values of the shape parameters used in simulations. (The unit for length parameters is  $\mu\text{m}$ .)

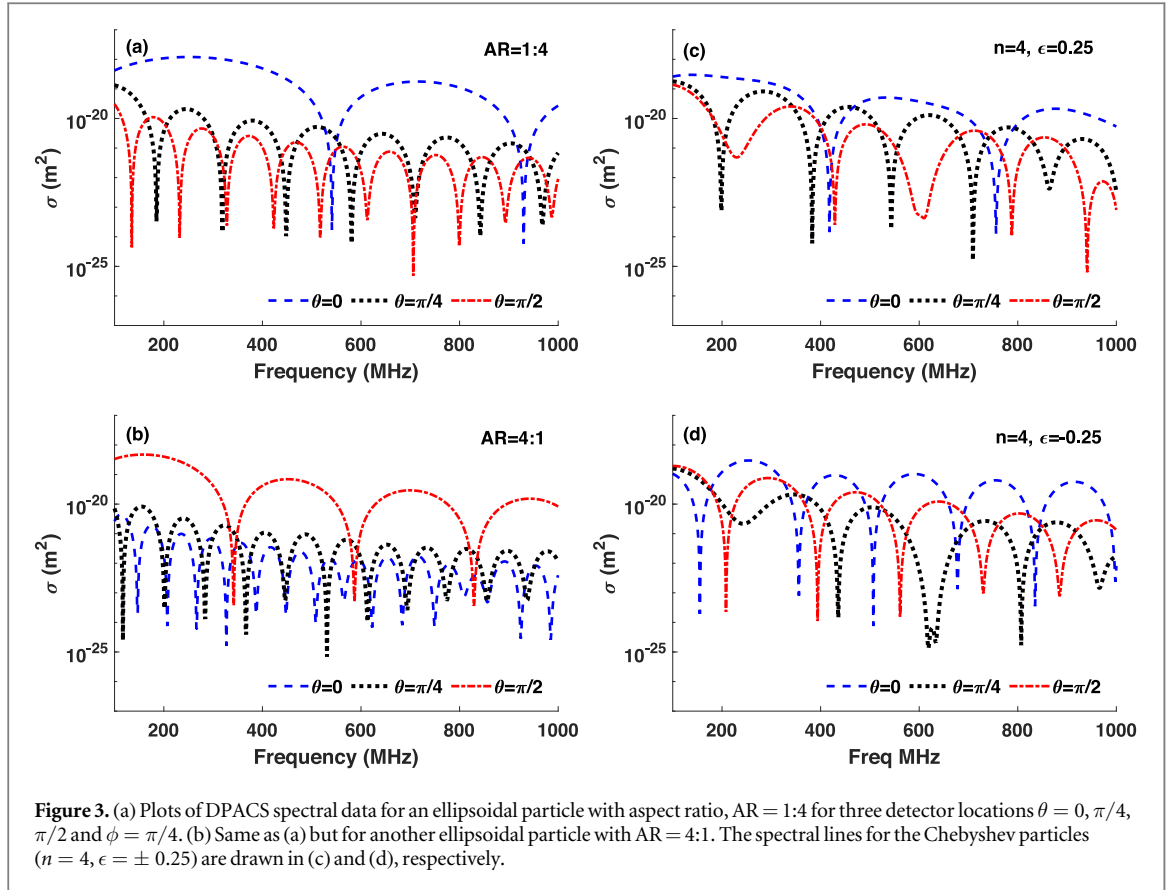
Objects	Volume ( $\mu\text{m}^3$ )	Shape parameters
Spheroids	523.6	b:a = 1:8, 1:4, 1:2, 2:1, 4:1, 8:1
Chebyshev particles	523.6	$\epsilon = \pm 0.25$ , $n = 2, 4$ and $6$
RBC	105	$\epsilon = \pm 0.05$ , $n = 35$ and $45$
ST	105	$D = 7.65$ , $t/2 = 0.70$ , $h/2 = 1.42$ , $d = 0.7D$
SC	105	$D = 6.37$ , $t/2 = 1.36$ , $h/2 = 1.47$ , $d = 0.7D$
EC	105	b:a = 1:1 b:a = 7:11

$n = 35, 45$  and deformation parameters,  $\epsilon = \pm 0.05$  were also employed. These are higher order Chebyshev particles [31]. The volume for each particle (ellipsoidal and Chebyshev) was fixed at  $523.6 \mu\text{m}^3$ . Table 2 (rows 3–5) illustrates these numerical values. The ellipsoidal particles are the simple particles. The corresponding DPACS spectra are also simple and easy to interpret. The aspect ratio was arbitrarily chosen for these particles. The ellipsoidal droplets were considered in this study to gain insights. The shape complexity of the Chebyshev particles grows with the increase of  $n$ . This class of particles was utilized previously by others to model realistic sources. The choice of the deformation parameters was made based on the previous works [28, 31].

The volume for normal and pathological RBCs was taken as  $105 \mu\text{m}^3$ . Figure 1 (left panel) displays the surface plots of these cells. The four morphological parameters for normal RBC as given in table 2 (row 6) were taken from the literature [30]. These values provided  $\eta = 2.66$  and  $\zeta = 2.75$  which were used to construct the discocyte (normal RBC) while evaluating equation (15). The shape resembling stomatocyte (ST) was generated by altering  $\eta$  and  $\zeta$  phenomenologically. For this shape, the upper half was simulated using equation (15) for  $\eta = 2.04$  and  $\zeta = 2.45$ , and the lower half was considered as a half-sphere. Hereditary disorders, namely, spherocyte (SC) and elliptocyte (EC) were considered in this work too and the corresponding numerical values of the shape parameters are given in table 2 (rows 8–9), respectively. The SC might be thought of as the equivalent sphere for normal RBC. The AR of EC was fixed based on the published results [11].

### 3.4. Numerical calculation

The DPACS was calculated for various nonspherical axisymmetric shapes by evaluating equation (5). The frequency range was considered as 100–1000 MHz with a step size of 1 MHz. Essentially, the DPACS was evaluated for three detector locations [ $\theta = 0, \pi/2, \pi/4$  but at constant  $\phi$  ( $\phi = \pi/4$ )] to examine how it would vary for different probing angles. However, the morphological parameters of the source were obtained by fitting the DPACS spectrum (computed along  $\theta = \pi/4$  and  $\phi = \pi/4$ ), which was arbitrarily chosen. The Monte Carlo integration method was employed to carry out the integration in equation (4) numerically [32]. Approximately, 20 million random points were thrown within a box enclosing each shape at a time to obtain converging result. For example, the size of the box was  $11 \times 11 \times 11 \mu\text{m}^3$  for a sphere of radius  $5 \mu\text{m}$ , which was placed at the center of the box while calculating the PA field. The fields corresponding to the random points that lied inside the shape were summed up to calculate the resultant field. Essentially, an array (to store complex pressure values) of length 901 was created at first and assigned with zeros. The field at a frequency for a valid throw was calculated [see equation (4)] and added with its previous value that was already stored in the array. This step was performed for all frequencies for that throw. In this way, computed fields for all valid throws were summed up for each frequency. Therefore, although we considered 20 million random points, memory requirement was small because only pressure values at 901 frequency points were stored. A personal computer (OS- Windows 10,



RAM- 12 GB, i5 processor, 3.30 GHz clock speed) was used to calculate the frequency dependent DPACS. The execution time for the same over a wide frequency range (100–1000 MHz) was estimated to be  $\approx 10$  minutes.

After that the DPACS spectrum (for  $\theta = \pi/4, \phi = \pi/4$ ) for each particle was analyzed for morphological characterization. At first the frequency location at which the DPACS became maximum was identified (let  $f_m$ ) and then normalized DPACS spectrum was obtained as  $\frac{\sigma(f)}{\sigma(f_m)}$ . The following step was to change the fitting parameters iteratively associated with the TAEFF ( $Q_1, Q_2, Q_3$ ), CFF ( $\Gamma$  and  $L$ ), TFF ( $R_r$  and  $R_c$ ) models and at each step a normalized quantity defined as  $\frac{f^2 FF(f)}{f_m^2 FF(f_m)}$  was calculated over the same frequency bandwidth to fit the normalized DPACS spectrum.

A  $\chi^2$  test was performed to assess goodness of a fitting. The  $\chi^2$  is defined as [33],

$$\chi^2 = \sum_{i=1}^N \left[ \frac{\sigma(f_i)}{\sigma(f_m)} - \frac{f_i^2 FF^2(f_i)}{f_m^2 FF^2(f_m)} \right]^2 / \left[ 0.1 \times \frac{\sigma(f_i)}{\sigma(f_m)} \right]^2. \quad (16)$$

Standard deviation at each point was considered to be 10% (arbitrarily fixed) of that of the normalized spectrum. We stored all the combinations of fit parameters for each model for which  $\chi^2$  values were  $\leq 2 \times$  [minimum of  $\chi^2$ ]. After that mean and standard deviation were obtained for each shape parameter.

#### 4. Computational results

Frequency dependent DPACS (for  $\theta = 0, \pi/4, \pi/2$  and  $\phi = \pi/4$ ) for ellipsoidal shapes with AR = 1:4 and 4:1 are plotted in figures 3(a) and (b), respectively for a frequency range of 100–1000 MHz. The same graphs for the Chebyshev droplets (with parameters  $n = 4, \epsilon = 0.25$  and  $n = 4, \epsilon = -0.25$ ) are shown in figures 3(c) and (d), respectively. These plots contain several prominent maxima and minima [16, 19]. The spectrum of each particle is unique in each direction. The first dip for the ellipsoidal particle having AR = 1:4 appears at 541, 185, and 135 MHz, when computed along  $\theta = 0, \pi/4$  and  $\pi/2$ , respectively. Similar trend is also observed in the figures 3(b–d). The thickness of the particle along the direction of measurement decides the locations of minima. The thicker is the particle, earlier is the location of the first minimum. Illustrative curves of the frequency dependent DPACS are given in figure 4 for RBCs. The first minimum for each RBC appears at a unique location for each direction of measurement. The first minimum for normal RBC manifests at 633, 347, and 247 MHz for the three detectors ( $\theta = 0, \pi/4$  and  $\pi/2$ ), respectively. The dips are not prominent in the case of ST for  $\theta = 0$  [see

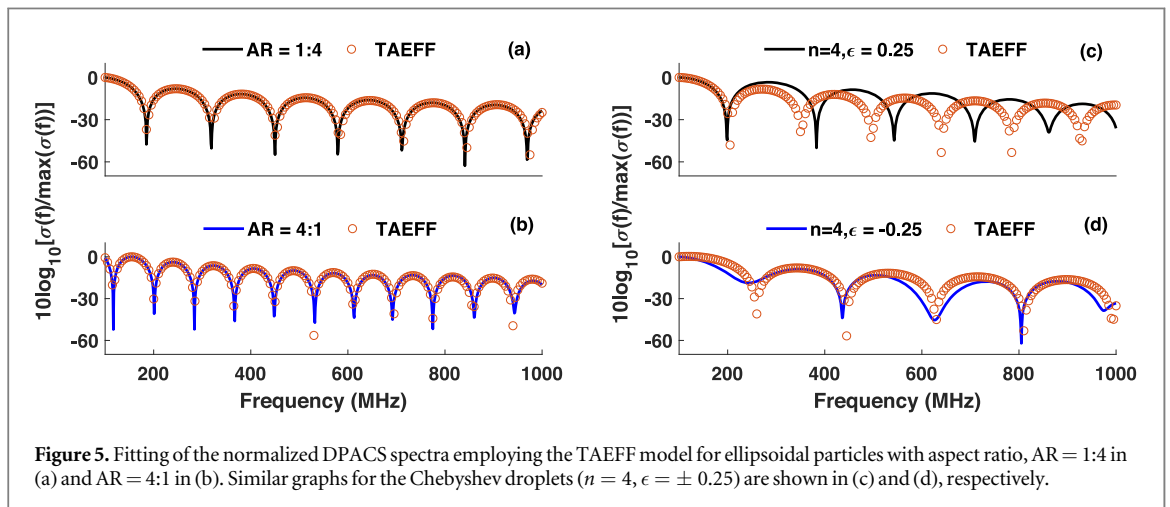
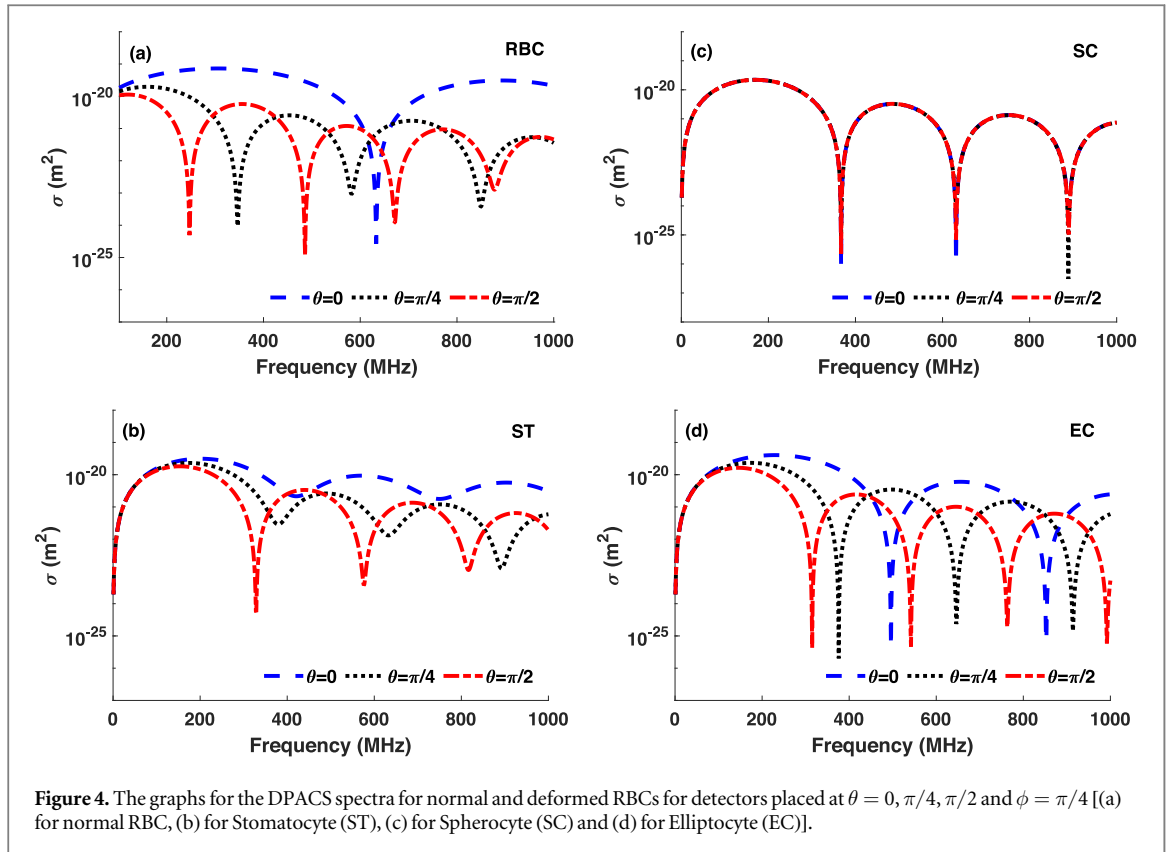


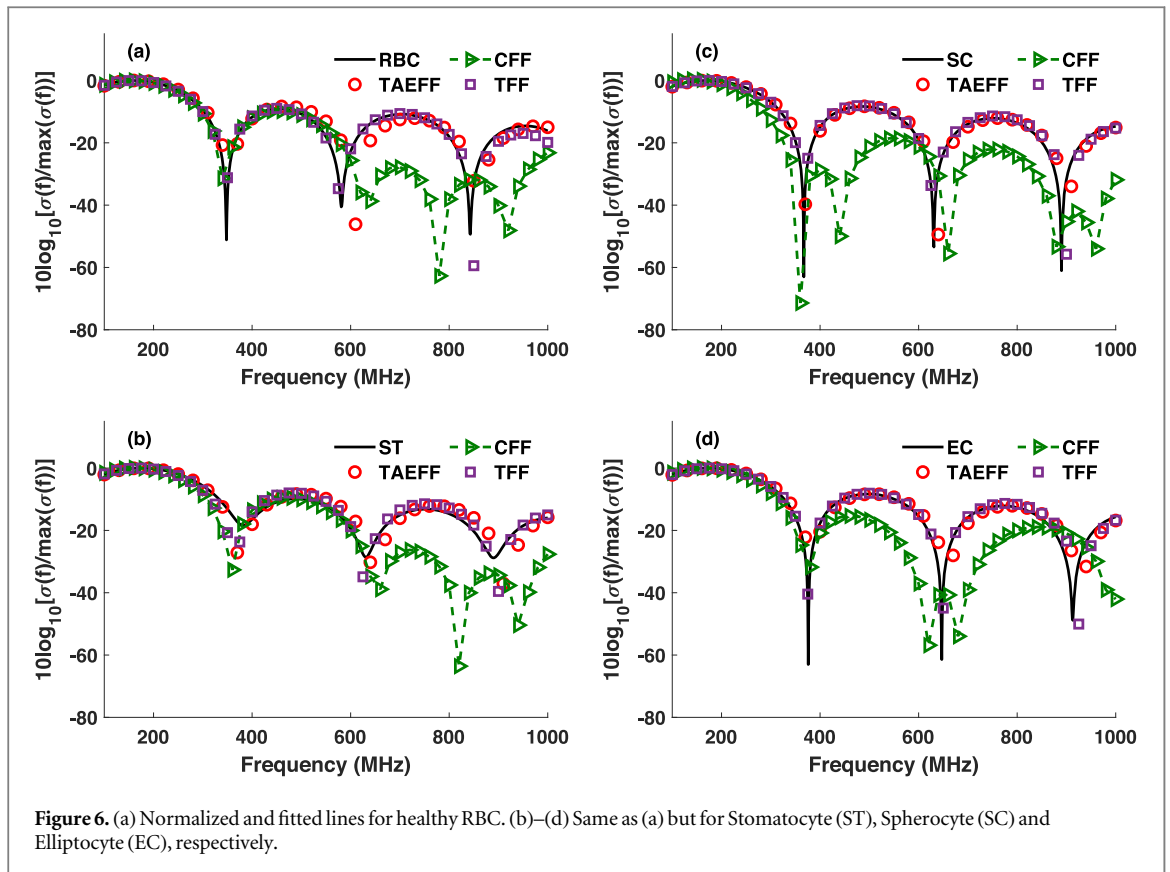
figure 4(b)]. The magnitudes of depths of the dips grow as we move from  $\theta = 0$  to  $\pi/2$ . The SC shape is essentially spherical, that is why the spectrum is identical from all detector locations. Figure 4(d) exhibits similar trend as that of figure 3(a) [because both are the oblate spheres].

Plots of normalized DPACSs are shown for ellipsoidal and Chebyshev particles in figure 5. The best fitted curves provided by the TAEFF model are also drawn in these figures. The numerical values of the best fit parameters and the corresponding values of  $\chi^2$  are given in table 3. Figures 5(a) and (b) demonstrate that the TAEFF model can accurately fit the simulated DPACS spectra over a wide frequency range (100–1000 MHz). That is why morphological parameters of the ellipsoidal particles are accurately retrieved (see rows 4, 6, 8, 10, 12 and 14, column 2, table 3). For each ellipsoidal particle, the percentage volume error is also inserted in the table. It is less than 4% for all particles.

The TAEFF model unable to accurately fit the spectrum for the Chebyshev particle with  $n = 4, \epsilon = 0.25$  particularly above  $\approx 380$  MHz [see figure 5(c)]. However, the fitting is much better in figure 5(d) over the entire frequency range. The  $\chi^2$  value corresponding to figure 5(c) is much higher than that of figure 5(d) though the volume error exhibits the opposite trend [as given in rows 17 and 27, column 2, table 3, respectively]. The

**Table 3.** The extracted values (mean  $\pm$  standard deviation) of the shape parameters for ellipsoid and Chebyshev particles. The actual values of the same parameters are also included here to assess the performance of the technique. The goodness of fitting ( $\chi^2$ ) and volume error (VE) are presented in the table as well. [The unit for  $a, b, R_c, \varrho_1, \varrho_2$  and  $\varrho_3$  is  $\mu\text{m}$ .]

Nominal values ( $\mu\text{m}$ )	Estimated values ( $\mu\text{m}$ ) $\theta = \pi/4, \phi = \pi/4$
$a = 6.28,$ $a = 6.28, b = 3.14$	$\chi^2 = 1.47e + 3, \text{VE} = 3.1\%$ $\varrho_1 = 6.25 \pm 0.53, \varrho_2 = 6.25 \pm 0.53,$ $\varrho_3 = 3.10 \pm 0.53$
$a = 7.93,$ $a = 7.93, b = 1.98$	$\chi^2 = 8.70e + 3, \text{VE} = 2.1\%$ $\varrho_1 = 7.90 \pm 0.53, \varrho_2 = 7.90 \pm 0.53,$ $\varrho_3 = 1.96 \pm 0.56$
$a = 10.0,$ $a = 10.0, b = 1.25$	$\chi^2 = 4.20e + 4, \text{VE} = 3.0\%$ $\varrho_1 = 9.97 \pm 0.55, \varrho_2 = 9.97 \pm 0.55,$ $\varrho_3 = 1.22 \pm 0.57$
$a = 3.96,$ $a = 3.96, b = 7.93$	$\chi^2 = 3.54e + 3, \text{VE} = 0.0\%$ $\varrho_1 = 3.97 \pm 0.58, \varrho_2 = 3.97 \pm 0.21,$ $\varrho_3 = 7.90 \pm 0.58$
$a = 3.14, a = 3.14,$ $b = 12.56$	$\chi^2 = 3.16e + 5, \text{VE} = 1.0\%$ $\varrho_1 = 3.14 \pm 0.58, \varrho_2 = 3.14 \pm 0.58,$ $\varrho_3 = 12.57 \pm 0.10$
$a = 2.50,$ $a = 2.50, b = 20.0$	$\chi^2 = 3.76e + 8, \text{VE} = 0.0\%$ $\varrho_1 = 2.50 \pm 0.58, \varrho_2 = 2.50 \pm 0.58,$ $\varrho_3 = 19.96 \pm 0.05$
$R_c = 5.31,$ $n = 2, \epsilon = 0.25$	$\chi^2 = 5.54e + 6, \text{VE} = 8.1\%$ $\varrho_1 = 4.00 \pm 0.58, \varrho_2 = 4.00 \pm 0.58,$ $\varrho_3 = 7.18 \pm 0.23$
$R_c = 4.93,$ $n = 4, \epsilon = 0.25$	$\chi^2 = 13.72e + 8, \text{VE} = 15.3\%$ $\varrho_1 = 5.26 \pm 0.08, \varrho_2 = 5.26 \pm 0.08$ $\varrho_3 = 5.21 \pm 0.04$
$R_c = 4.89,$ $n = 6, \epsilon = 0.25$	$\chi^2 = 2.40e + 9, \text{VE} = 13.8\%$ $\varrho_1 = 3.95 \pm 0.51, \varrho_2 = 3.95 \pm 0.51$ $\varrho_3 = 6.90 \pm 0.15$
$R_c = 5.00,$ $n = 35, \epsilon = 0.05$	$\chi^2 = 2.47e + 4, \text{VE} = 2.3\%$ $\varrho_1 = 5.21 \pm 0.78, \varrho_2 = 5.21 \pm 0.78$ $\varrho_3 = 4.71 \pm 0.46$
$R_c = 5.00,$ $n = 45, \epsilon = 0.05$	$\chi^2 = 4.29e + 5, \text{VE} = 1.7\%$ $\varrho_1 = 5.20 \pm 0.78, \varrho_2 = 5.20 \pm 0.78$ $\varrho_3 = 4.70 \pm 0.45$
$R_c = 4.53,$ $n = 2, \epsilon = -0.25$	$\chi^2 = 2.18e + 8, \text{VE} = 1.0\%$ $\varrho_1 = 5.85 \pm 0.53, \varrho_2 = 5.85 \pm 0.53$ $\varrho_3 = 3.63 \pm 0.50$
$R_c = 4.78,$ $n = 4, \epsilon = -0.25$	$\chi^2 = 4.92e + 6, \text{VE} = 45.0\%$ $\varrho_1 = 4.03 \pm 0.58, \varrho_2 = 4.03 \pm 0.58$ $\varrho_3 = 4.24 \pm 0.40$
$R_c = 4.82,$ $n = 6, \epsilon = -0.25$	$\chi^2 = 4.92e + 6, \text{VE} = 29.4\%$ $\varrho_1 = 6.36 \pm 0.51, \varrho_2 = 6.36 \pm 0.51,$ $\varrho_3 = 4.00 \pm 0.45$
$R_c = 5.00,$ $n = 35, \epsilon = -0.05$	$\chi^2 = 10.81e + 5, \text{VE} = 2.9\%$ $\varrho_1 = 5.22 \pm 0.79, \varrho_2 = 5.22 \pm 0.78,$ $\varrho_3 = 4.72 \pm 0.46$
$R_c = 5.00,$ $n = 45, \epsilon = -0.05$	$\chi^2 = 14.56e + 4, \text{VE} = 1.7\%$ $\varrho_1 = 5.20 \pm 0.78, \varrho_2 = 5.20 \pm 0.78,$ $\varrho_3 = 4.70 \pm 0.45$



volume errors for the intermediate Chebyshev particles are slightly higher because of their complex structures (see rows 17, 19, 27 and 29) than lower and very higher order particles (error is  $< 10\%$ ) as can be seen from table 3.

Plots of normalized DPACS corresponding to figure 4 (for  $\theta = \pi/4$  and  $\phi = \pi/4$ ) are presented in figure 6. The fitted curves generated by the TAEFF, CFF and TFF models are displayed in each figure as well (using mean values of  $\varrho_1$ ,  $\varrho_2$  and  $\varrho_3$  for the TAEFF;  $\Gamma$ ,  $L$  for the CFF;  $R_t$  and  $R_c$  for the TFF). The estimated and actual values of the shape parameters are presented in table 4. Figures 6(a)–(d) clearly illustrate that the TAEFF and TFF models in general facilitate excellent fits to the curves from 100–1000 MHz. The CFF model fits the curves accurately till the frequency 540, 260, 220 and 400 MHz in case of normal RBC, ST, SC and EC, respectively. Therefore, the performance of the CFF model is inferior than others.

Table 4 demonstrates (rows 4–6 and column 2) that the anticipated values of  $\varrho_1$  and  $\varrho_2$  are very close to the radius of normal RBC (deviation is  $\approx 3\%$ ). The estimated value of  $\varrho_3$  lies between  $t = 1.4 \mu\text{m}$  (minimum height of RBC) and  $h = 2.84 \mu\text{m}$  (maximum height of RBC). The extracted value of  $\Gamma$  (rows 4, column 3) is close to the physical value (error  $\approx 2\%$ ) and  $L$  is comparable to the highest thickness  $h = 2.84 \mu\text{m}$  of the cell (error  $\approx 4\%$ ). The distance of the outer periphery from the center (*i.e.*,  $R_t + R_c$ ) is appropriately anticipated by the TFF model (error  $\approx 2\%$ ). However, the thickness of the estimated toroid is slightly higher than the maximum thickness of normal RBC. The TAEFF and TFF models offer better curve fitting than the CFF model for normal RBC (see  $\chi^2$  values at row 3, columns 2, 3 and 4 of table 4). As expected the TAEFF model works much better for the last two cases (error  $\leq 6\%$ ) in comparison to the second case (stomatocytosis, error  $< 15\%$ ). The CFF model performs better for first two cells than the others. For all the deformed cells, volume errors associated with the TFF model are comparable.

Numerous PA spectral lines produced by a number of droplets are illustrated in this work (see figures 3 and 4). However, in practice, these spectra are obtained by taking the Fourier transform of the corresponding PA signals. Some representative PA signals are displayed in figure 7. A narrow and sharp N-shaped pulse is computed when the ultrasonic transducer is positioned at  $\theta = 0$  as given in figure 7(a). The pulse is elongated by a factor of 1.66 and 2, when probed from  $\theta = \pi/4$  and  $\pi/2$ , respectively. Its amplitude is approximately reduced by a factor of 3.15 and 4.14 when probed from the same directions, respectively. This can be attributed to the fact that RBC is thinner when viewed by the ultrasound detector from the first direction compared to the second and third directions. The amplitude of the PA signal is reduced by a factor of  $\approx 2.5$  when measured from the direction of  $\theta = \pi/4$  and  $\pi/2$  in case of ST compared to that of  $\theta = 0$ . As anticipated, signals are identical for SC from all directions as shown in figure 7(c). A positive pressure followed by a negative pressure sequence trend is also

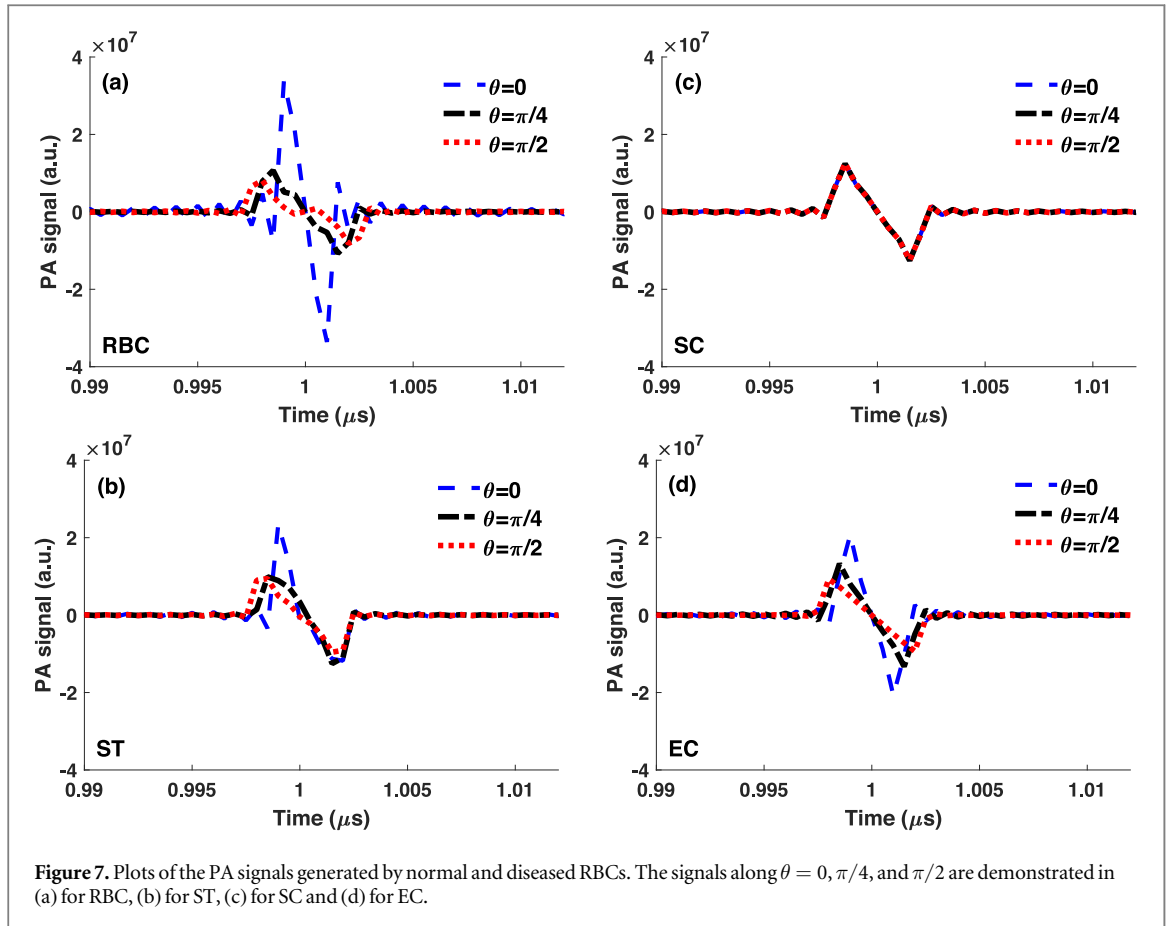
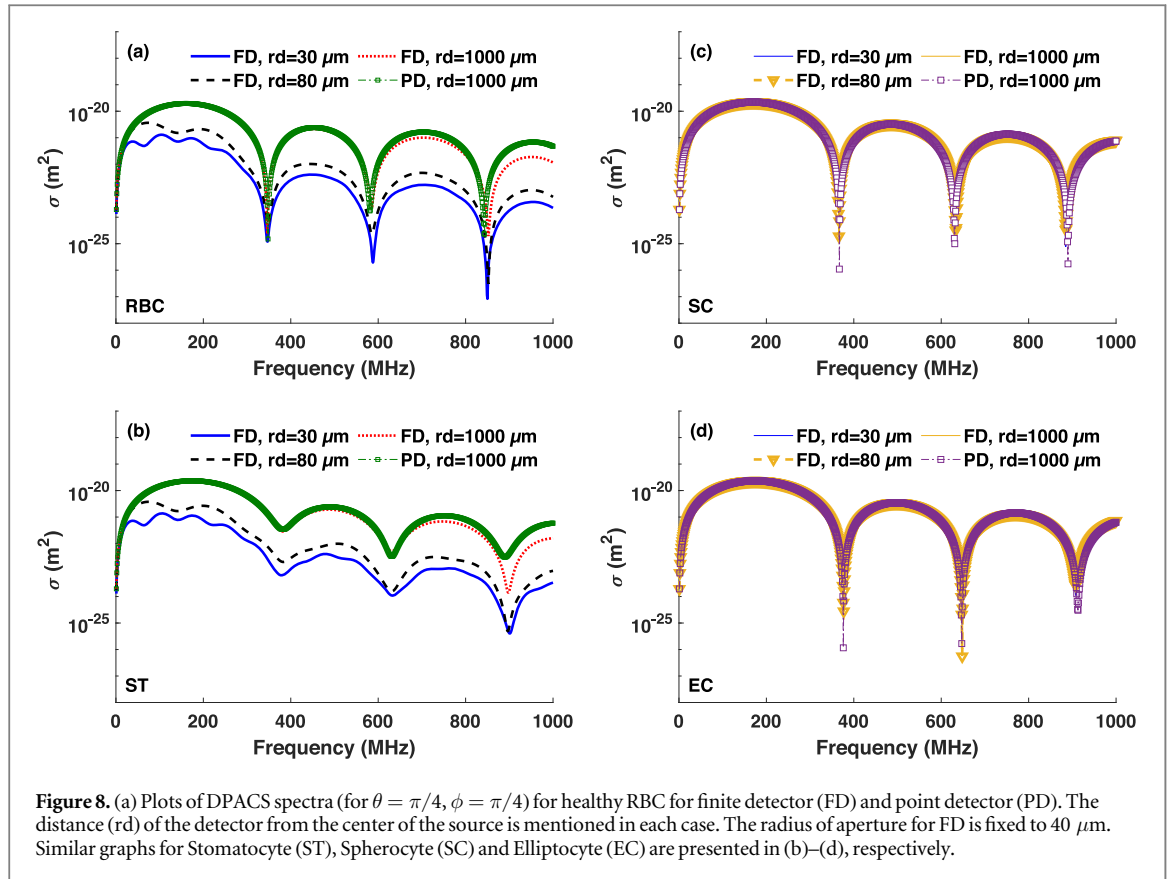


**Table 4.** The evaluated values (mean  $\pm$  standard deviation) of the morphological parameters for healthy and pathological cells examined in this work. The nominal values of those parameters are appended here too for comparison. The goodness of fitting ( $\chi^2$ ) and volume error (VE) are also given in the table. [The unit for  $R_e, h, t, \varrho_1, \varrho_2, \varrho_3, \Gamma, L, R_t$  and  $R_c$  is  $\mu\text{m}$ .]

Nominal values	Estimated values ( $\mu\text{m}$ )		
	TAEFF	CFF	TFF
$R_e = 3.82$ $t/2 = 0.7$ $h/2 = 1.42$	$\chi^2 = 9.00e + 5$ $\varrho_1 = 3.94 \pm 0.73$ $\varrho_2 = 3.94 \pm 0.73$ $\varrho_3 = 1.67 \pm 0.56$ VE=3.4%	$\chi^2 = 9.00e + 6$ $\Gamma = 3.75 \pm 0.02$ $L = 2.72 \pm 0.10$ VE=13.8%	$\chi^2 = 5.81e + 5$ $R_t = 2.12 \pm 0.01$ $R_c = 1.62 \pm 0.03$ VE=4.5%
$R_e = 3.18$ $t/2 = 1.36$ $h/2 = 1.47$	$\chi^2 = 2.52e + 4$ $\varrho_1 = 3.70 \pm 0.80$ $\varrho_2 = 3.70 \pm 0.80$ $\varrho_3 = 1.56 \pm 0.56$ VE=14.8%	$\chi^2 = 7.12e + 04$ $\Gamma = 3.63 \pm 0.11$ $L = 2.58 \pm 0.30$ VE=1.72%	$\chi^2 = 3.94e + 4$ $R_t = 2.04 \pm 0.03$ $R_c = 1.47 \pm 0.02$ VE=17.1%
$a = 2.92$ $a = 2.92$ $b = 2.92$	$\chi^2 = 7.14e + 2$ $\varrho_1 = 2.99 \pm 0.56$ $\varrho_2 = 2.99 \pm 0.56$ $\varrho_3 = 2.77 \pm 0.38$ VE=1.9%	$\chi^2 = 7.00e + 7$ $\Gamma = 3.59 \pm 0.02$ $L = 4.79 \pm 0.13$ VE=84.7%	$\chi^2 = 7.58e + 7$ $R_t = 2.03 \pm 0.01$ $R_c = 1.47 \pm 0.02$ VE=17.5%
$a = 3.40$ $a = 3.40$ $b = 2.16$	$\chi^2 = 6.56e + 2$ $\varrho_1 = 3.36 \pm 0.55$ $\varrho_2 = 3.36 \pm 0.55$ $\varrho_3 = 2.09 \pm 0.50$ VE=5.9%	$\chi^2 = 11.74e + 7$ $\Gamma = 3.46 \pm 0.04$ $L = 3.43 \pm 0.47$ VE=22.8%	$\chi^2 = 2.08e + 6$ $R_t = 1.97 \pm 0.01$ $R_c = 1.43 \pm 0.01$ VE=24.2%



observed for EC as shown in figure 7(d). The N-shaped signals for  $\theta = \pi/4$  and  $\pi/2$  are slightly broader than that of  $\theta = 0$ .

## 5. Discussion and conclusions

The Green's function approach has been used to solve the Helmholtz equation. This equation accurately models the production and propagation of the PA waves. The PA fields have been calculated for ellipsoidal droplets, Chebyshev particles, normal and diseased RBCs. The DPACS spectra have also been computed for the above mentioned droplets. Thicker is the particle (along the direction of estimation), greater is the number of fluctuations in the DPACS curve. The location of the first minimum appears earlier as the thickness of the PA absorber grows in the same direction. Also the amplitude of the DPACS increases with the expansion of the area normal to the direction of observation. Further, the TAEFF, CFF and TFF models are employed to fit the DPACS curves.

The TAEFF model extracts volume information accurately even for complex structures. This is because, three parameters, providing more degrees of freedom, can be tuned efficiently to obtain better fitting in comparison to the CFF and TFF models which have two degrees of freedom. The CFF model works satisfactorily for particles with approximately cylindrical shape. It can be readily understood that the horn torus ( $R_t = R_c$ ) better mimics the shape of normal RBC. However, in this work, we have found that the ring torus ( $R_t > R_c$ ) provides better fitting to the DPACS spectrum for normal RBC. This may be attributed to the fact that the central region of normal RBC contributes less to the DPACS (because it is very thin around the centre but thick close to the periphery) and it is ensured in case of ring torus. It may be emphasized that we did not consider normalized  $\chi^2$  herein. Further, DPACS at some frequencies (at the locations of dips) became very small and that is why  $\chi^2$  became very large in some cases. Therefore, a large value of  $\chi^2$  did not always mean that the fitting was poor.

In this work, it was assumed that the detector was an ideal point detector having uniform sensitivity between 100 to 1000 MHz. The measurements are carried out using bandlimited detectors during experiment and thus more than one detector would be required to record signals between 100 to 1000 MHz. Further, simulated PA spectra are devoid from electrical and thermal noises, which in general appear in practice. Note that measurements are performed using detectors with finite aperture. Keeping this in our mind, we exhaustively calculated DPACS spectra (for  $\theta = \pi/4$ ,  $\phi = \pi/4$ ) for different RBCs for finite size detectors (see figure 8). The

DPACS was computed at three different radial distances (30, 80, and 1000  $\mu\text{m}$ ). The radius of the aperture of the detector was fixed at 40  $\mu\text{m}$ . The DPACS spectrum for a point detector is also included in each figure for comparison. It can be observed from figures 8(a) and (b) that the deep nulls that appear in the DPACS plots for a finite size detector have been reduced and become little wide for normal RBC and ST, respectively. However, there is no much variation can be seen in case of SC and EC as evidenced from figures 8(c) and (d). Nevertheless, the effect of directivity of the sensor (because of finite aperture size) on DPACS spectrum was not included while calculating it. Further investigation is required to study this aspect.

It may be noted that attenuation is a major issue at high frequencies. We have considered attenuation of acoustic waves in another work in details [19]. We found that DPACS spectrum decays exponentially due to attenuation. However, we used attenuation compensated DPACS spectrum while solving the inverse problem and thus reliable estimates of the shape parameters were obtained. Moreover, in this work, we took only one orientation of the PA source with respect to the co-ordinate system and accordingly, computation was performed. Hence, intravariability of shape of a particular class of particles (e.g., normal RBC) was not incorporated in this study. In reality, orientation of a source under investigation might be arbitrary and therefore, DPACS spectrum averaged over many orientations is obtained for further analysis [7]. This issue has been recently dealt by us and presented in details in [19].

In this study, we considered axisymmetric shapes only. It will be very interesting to study the variation of the DPACS with frequency for nonspherical and nonaxisymmetric particles. Specially, echinocyte cell which is clinically very important and falls in the category of nonspherical and nonaxisymmetric particles. These shapes can be generated by spherical harmonics expansion [34, 35]. It will also be interesting to apply the inverse problem framework presented here for acoustically inhomogeneous source and subsequently, examine the performance of the form factor models in estimating morphological parameters.

In conclusion, the frequency dependent DPACS in the far field has been computed (for three angular locations  $\theta = 0, \pi/4, \pi/2$  and  $\phi = \pi/4$ ) for some nonspherical axisymmetric fluid particles resembling biological cells for an ideal point detector having constant sensitivity over the frequency range from 100 to 1000 MHz. The DPACS spectra for  $\theta = \pi/4$  and  $\phi = \pi/4$  have been fitted with the TAEFF, CFF and TFF models to obtain the size and shape information of the PA objects. In general, the TAEFF model works well for all shapes. This technique may be employed in practice for morphological characterization of normal and pathological RBCs.

## Acknowledgments

The computational results reported in this work were partially performed on the Central Computing Facility of IITA, Allahabad. The authors are grateful to the members of BMIL for their cooperation during this work.

## Disclosures

The authors pronounce no irreconcilable circumstances. No funding is received for this work.

## ORCID iDs

Ratan K Saha  <https://orcid.org/0000-0001-7274-6707>

## References

- [1] Cai C *et al* 2016 *In vivo* photoacoustic flow cytometry for early malaria diagnosis *Cytometry Part A* **89A** 531–42
- [2] Galanzha E I and Zharov V P 2013 Circulating tumor cell detection and capture by photoacoustic flow cytometry *in vivo* and *ex vivo* *Cancers* **5** 1691–731
- [3] Cai C *et al* 2016 Photoacoustic flow cytometry for single sickle cell Detection *in vitro* and *in vivo* *Analytical Cellular Pathology* **2642361** 1–11
- [4] Wang L V 2009 *Photoacoustic Imaging and Spectroscopy* (Boca Raton, : CRC Press) 37–46
- [5] Warbal P, Pramanik M and Saha R K 2019 Impact of sensor apodization on the tangential resolution in photoacoustic tomography, *J. Opt. Soc. Am. A* **36** 245–52
- [6] Strohm E M, Berndl E S L and Kolios M C 2013 Probing red blood cell morphology using high-frequency photoacoustics *Biophys J.* **105** 59
- [7] Strohm E M, Berndl E S L and Kolios M C 2013 High frequency label free photoacoustic microscopy of single cells *Photoacoustics* **1** 49
- [8] Moore M J, Sebastian J A and Kolios M C 2019 Determination of cell nucleus-to-cytoplasmic ratio using imaging flow cytometry and a combined ultrasound and photoacoustic technique: a comparison study *J. Biomed Opt.* **24** 106502
- [9] Li H, Lu L, Buffet P A, Dao M, Karniadakis G and Suresh S 2018 Mechanics of diseased red blood cells in human spleen and consequences for hereditary blood disorders *Proc. Natl. Acad. Sci. USA* **115** 9574

- [10] Kim J, Lee H and Shin S 2015 Advances in the measurement of red blood cell deformability: a brief review *Journal of Cellular Biotechnology* **1** 63–79
- [11] Costa L D, Galimand J, Fenneteau O and Mohandas N 2013 Hereditary spherocytosis, elliptocytosis, and other red cell membrane disorders *Blood Rev.* **27** 167
- [12] Pivkin I V, Peng Z, Karniadakis G E, Buffet P A, Dao M and Suresh S 2016 Biomechanics of red blood cells in human spleen and consequences for physiology and disease *Proc. Natl. Acad. Sci. USA* **113** 7804–9
- [13] Simon P, Frankowski M, Bock N and Neukammer J 2016 Label-free whole blood cell differentiation based on multiple frequency AC impedance and light scatter analysis in a micro flow cytometer *Lab Chip* **16** 2326–38
- [14] Gienger J, Gross H, Ost V, Bär M and Neukammer J 2019 Assessment of deformation of human red blood cells in flow cytometry: measurement and simulation of bimodal forward scatter distributions *Biomedical Opt. Express* **10** 4531–50
- [15] Gibaud E 2015 Numerical simulation of red blood cells flowing in a blood analyzer *PhD Thesis* Université Montpellier
- [16] Saha R K, Karmakar S, Adhikari A and Kolios M C 2017 Photoacoustic field calculation for nonspherical axisymmetric fluid particles *Biomed. Phys. Eng. Exp.* **3** 015017
- [17] Kaushik A, Sonker D and Saha R K 2019 Study on angular distribution of differential photoacoustic cross-section and its implication in source size determination *J. Opt. Soc. Am. A* **36** 387–96
- [18] Kaushik A, Sonker D and Saha R K 2019 Use of angular distribution of differential photoacoustic cross-section data for estimating source size *Proc. of SPIE-OSA* **11077** 110770E-1
- [19] Kaushik A, Paul A and Saha R K 2020 A systematic analysis of frequency dependent differential photoacoustic cross-section data for source size estimation *J. Opt. Soc. Am. A* **37** 1895
- [20] Kaushik A, Yallavarthy P K and Saha R K 2020 Convergent Born series improves accuracy of numerical solution of time independent photoacoustic wave equation *J. Mod. Opt.* **67** 1–7
- [21] Saha R K 2020 Numerical solution to the time independent inhomogeneous photoacoustic wave equation using the Born series methods *J. Opt. Soc. Am. A* **37** 1907–15
- [22] Diebold G J, Sun T and Khan M I 1991 Photoacoustic monopole radiation in one, two and three dimensions *Phys. Rev. Lett.* **67** 3384–7
- [23] Morse P M and Feshbach H 1953 Methods of theoretical physics *McGraw-Hill Chapter 7* 791–895
- [24] Alves C and Oliveira C L P 2018 Calculation of small angle scattering patterns *Small Angle Scattering and Diffraction* (Rijeka: IntechOpen)
- [25] Schroer M A 2011 Small angle x-ray scattering studies on proteins under extreme conditions *PhD Thesis* Universitätsbibliothek Technische Universität Dortmund Chapter 2
- [26] Folrster S *et al* 1999 Fusion of charged block copolymer micelles into toroid networks *J. Phys. Chem. B.* **103** 6657–68
- [27] Lindner P and Zemb T 2002 Modelling of small-angle scattering data from colloids and polymer systems, *Neutrons, X-Rays and Light* (Amsterdam: Elsevier) 16 391–420
- [28] Mugnai A and Wiscombe W J 1986 Scattering from nonspherical Chebyshev particles. I: cross sections, single-scattering albedo, asymmetry factor and backscattered fraction *Appl. Opt.* **25** 1235–44
- [29] Funaki H 1955 Contributions on the shapes of red blood corpuscles *The Japanese Journal of Physiology* **5** 81–92
- [30] Bi L and Yang P 2013 Modeling of light scattering by biconcave and deformed red blood cells with the invariant imbedding T-matrix method *J. Biomed. Opt.* **18** 055001
- [31] Rother T, Schmidt K, Wauer J, Shcherbakov V and Gayet J 2006 Light scattering on Chebyshev particles of higher order *Appl. Opt.* **45** 6030–7
- [32] Pharr M and Humphreys G 2014 Physically-based image synthesis: from theory to implementation *Elsevier Chapter 14* 497–520
- [33] Oliveira C L P 2011 Investigating macromolecular complexes in solution by small angle x-ray scattering *Current Trends in X-Ray Crystallography* (Rijeka: IntechOpen)
- [34] Khairy K and Howard J 2008 Spherical harmonics-based parametric deconvolution of 3D surface images using bending energy minimization *Med. Image Anal.* **12** 217–27
- [35] Khairy K, Foo J and Howard J 2010 Shapes of red blood cells: comparison of 3D confocal images with the bilayer-couple model *Cell Mol. Bioeng.* **1** 173–81